ORIGINAL RESEARCH ARTICLE

Effect of Tensile Direction on Corrosion Behavior of AZ31 Magnesium Alloy Rolled Sheets

Tingzhuang Han, Lifei Wang, Ye Lu, Liwei Lu, and Hanuma Reddy Tiyyagura

The influence of pre-tensile deformation at different directions on the corrosion properties of AZ31 rolled sheet has been investigated. Uniaxial tensile test with the strain of 6% has been carried out at angles of 0°, 15°, 30°, 45°, 60°, 75° and 90° with rolling direction (RD), respectively. The corrosion behavior of specimens with different deformation directions in 3.5% NaCl solution and 8.5% Na_2SO_4 solution was measured by immersion test, potentiodynamic polarization method and electrochemical impedance spectroscopy. After immersion tests, the surface characteristics of various specimens were investigated by scanning electron microscope (SEM). Results showed that the tensile directions had a significant influence on the corrosion behavior. With the increase of the angle between tensile direction and RD, the hydrogen evolution rate in the 3.5% NaCl increased first and then decreased. The turning point was A45 specimen with the minimum value of 2.1 mm/y. The similar trends were also observed in the 8.5% Na_2SO_4 solution. In electrochemical testing, the A45 specimen exhibited the best corrosion resistance with the largest diameter of the impedance arc and lowest self-corrosion current. The further the angle of the specimen deviated from 45° direction, the lower corrosion resistance.

1. Introduction

Magnesium and its alloys are widely used in electronic, automotive, biomedical industries and other fields because of their high specific strength, low density and biocompatibility (Ref 1-4). The wrought magnesium alloys with uniform microstructure exhibited better mechanical properties (high strength and ductility) than that of as-cast magnesium alloys, which was expected to realize industrial application. However, the high corrosion rate of wrought magnesium alloys limited their wide application in a large extent. As is well known, the corrosion resistance of metals was closely related to crystal orientation (Ref 5-8), especially for magnesium alloys with hexagonal closest packed (HCP) crystal structures (Ref 9).

The Mg alloys with strong (0001) basal texture formed by extrusion or hot rolling usually exhibited orientation-dependent characteristic, where different orientations of the lattice resulted in some differences in corrosion properties. Liu et al. (Ref 10) studied the effects of crystallographic orientation on the corrosion behavior of pure magnesium in 0.1N HCl and concluded that the grains with c-axis near < 0001 > had the best corrosion resistance measured by EBSD and AFM. Xu et al. (Ref 11) also explained that compared to that of the surface only composed of prismatic plane, galvanic corrosion could reduce the corrosion resistance with a surface composed of both prismatic planes and basal planes. Moreover, many other studies have confirmed that the corrosion behavior of the base material and the protectiveness of the corrosive film both are dependent on the crystallographic texture (Ref 12).

In addition, inducing deformation twins in magnesium alloys was an important way to strengthen the basal texture (Ref 13). Due to the effects of twins on orientations changing, Mg alloy sheets with tensile twins and compressive twins were extensively studied. The different orientations of the lattices in the twin region resulted in different properties comparing to that of the surrounding matrix (Ref 13, 14). In recent studies, the researchers mainly focused on the effects of twinning on the mechanical properties of the alloys, while the influence on the corrosion behavior was less in consideration. Elizer et al. (Ref 15) investigated the effect of the equal channel angular pressing (ECAP) on the corrosion behavior of AZ31 magnesium alloy. The results showed that the ECAP treatment induced a higher density of dislocations and twins in magnesium alloys, leading to a significant reduction in the corrosion resistance. Zhou et al. (Ref 16) investigated the corrosion resistance of rolled AZ31B alloy sheets with and without twins by changing the heat treatment temperatures. The results showed that corrosion was more severe in highly twinned tissue than that in specimens with almost no twinning. According to Stanford et al. (Ref 17) and Sarker et al. (Ref 18), the orientation relationship of twinned crystals was highly energy-determining, but in general

Tingzhuang Han, Department of Aviation Manufacturing Engineering, Changzhou Institute of Technology, Changzhou 213032, China; **Lifei Wang** and **Ye Lu**, Shanxi Key Laboratory of Advanced Magnesium-Based Materials, College of Materials Science and Engineering, Taiyuan University of Technology, Taiyuan 030024, China; **Liwei Lu**, Hunan Provincial Key laboratory of High Efficiency and Precision Machining of Difficult-to-Cut Material, Hunan University of Science and Technology, Xiangtan 411201 Hunan, People's Republic of China; and **Hanuma Reddy Tiyyagura**, Rudolfovo–Science and Technology Centre Novo Mesto, Podbreznik 15, 8000 Novo Mesto, Slovenia. Contact e-mail: wanglifei@tyut.edu.cn.

the energy of the atoms in the twinned region was greater than that of the atoms in normal lattice positions. This could also explain why corrosion was more likely to occur in the twin zone, as the presence of twin structures affected the corrosion behavior of magnesium alloys. Atoms in the twin crystal region were thought to have higher atomic activity than those in the normal lattice region. Wang et al. (Ref 19) suggested that twinning caused galvanic corrosion in magnesium alloys, which was one of the main drivers of early corrosion. Therefore, the presence of twins on the outer surface will negatively affect the corrosion behavior.

Previous researches had focused on how crystal orientation affects the corrosion behavior of magnesium alloys. While Mg alloy rolled sheets usually exhibit obvious anisotropy, the microstructure would be also different in different directions. Thus, in order to investigate the influence of tensile deformation at different directions on corrosion properties, uniaxial tensile tests of AZ31 alloy rolled sheets were carried out at angles of 0°, 15°, 30°, 45°, 60°, 75° and 90° with rolling direction (RD), respectively. And the tensile strain was set at 6%. Corrosion resistance of AZ31 alloy sheets was examined in 3.5 wt.% NaCl solution and 8.5% Na_2SO_4 solution according to immersion test and potentiodynamic polarization measurement. The microstructure evolution and corrosion properties were characterized and compared.

2. Experimental Methods

2.1 Samples Preparation

In this study, commercially AZ31 magnesium alloy rolled sheets with initial 1mm thickness were used. The as-received AZ31 rolled sheets were annealed at 400 °C for 4h prior to the experiments. The tensile specimens were machined into 22×15 mm (gauge length and width) and then ground with 800, 1200, 1400 and 2000 girt SiC paper and polished by Al_2O_3 solution before tension tests. The strain rate was set as 2.78×10^{-4} s^{-1}, and the degree of tensile deformation was 6%. The tensile directions were set at angles of 0, 15, 30, 45, 60, 75 and 90° to the RD. These samples were designated as RD, A15, A30, A45, A60, A75 and A90, respectively. To minimize the effect of errors on the results, each experiment was performed three times.

2.2 Material Characterization

Metallographic images were obtained by optical microscopy (OM, Leica DM2700). Field emission scanning electron microscopy (SEM, Tescan Mira 3) was used to observe the surface morphology and cross sections after corrosion.

2.3 Hydrogen Evolution Testing

The corrosion rate of magnesium alloy is measured by immersion test (Ref 20). The samples were immersed in 3.5 wt.% NaCl solution and 8.5 wt.% Na_2SO_4 for 7 days at 25 °C with the size of 15mm (tensile direction) × 10mm × 1mm. The funnel was placed upside down in the beaker, and the hydrogen produced in the reaction was collected through the funnel in the upper dropper. The ratio of the surface area of the sample (cm^2) to the volume of the solution (ml) was set at 1/150 in order for the magnesium alloy to react adequately. The corrosion rate P_H (mm/year) and P_w (mm/year) was measured by Eq 1 and 2 (Ref 20):

$$P_H = 2.008 \times \frac{V_H}{At} \tag{Eq 1}$$

$$P_W = 2.1 \times \frac{W_a - W_b}{At} \tag{Eq 2}$$

where V_H (mL) is the volume of evolved hydrogen, A (cm^2) is the sample surface area and t (day) refers to the immersion duration. After immersed for 7 days, the samples were taken out and the surface corrosion products were removed with chromic acid solution (AgNO$_3$ 10g/L, CrO$_3$ 100g/L). The samples after corrosion were then weighed on an analytical balance after being washed in alcohol and observed with a scanning electron microscope.

2.4 Electrochemical Testing

The electrochemical experiments were carried out with a standard three-electrode cell using the CHI660E electrochemical system. Open-circuit potential (OCP) tests were performed in the 1800s to achieve a balanced electrochemical state. The frequency range was of AC impedance was chosen from 100 kHz to 100 mHz, an amplitude of 5 mV and 12 points per order of magnitude. The ZSimpWin software was used to fit the equivalent circuit and calculate key data such as polarization resistance (R_p) and double-layer capacity (C_{dl}) to evaluate the corrosion system. After holding at open-circuit potential (OCP) for 1800 s to reach steady state, the potentiodynamic polarization curve was measured at a scan rate of 10 mV s^{-1}.

3. Results and Discussion

3.1 Microstructural Characterization

All the samples taken from rolled sheets were annealed at 400 °C for 4 h before the experiments. The uniform microstructure was obtained with increased grain size after annealing at 400 °C (Ref 21). As shown in Fig. 1, the yield strength (YS) of samples in different directions gradually increased with the increase in angle between the tensile direction and RD. During the tensile deformation, the main deformation mechanisms included basal slip, prismatic slip and pyramidal < c + a > slip systems. For the rolled magnesium alloy sheets, the c-axes of most grains are almost parallel to the normal direction (ND) and tilted slightly to RD. The activation of basal slip from tension in RD is greater than that during tension in TD (Ref 22). As the basal slip is most likely to be
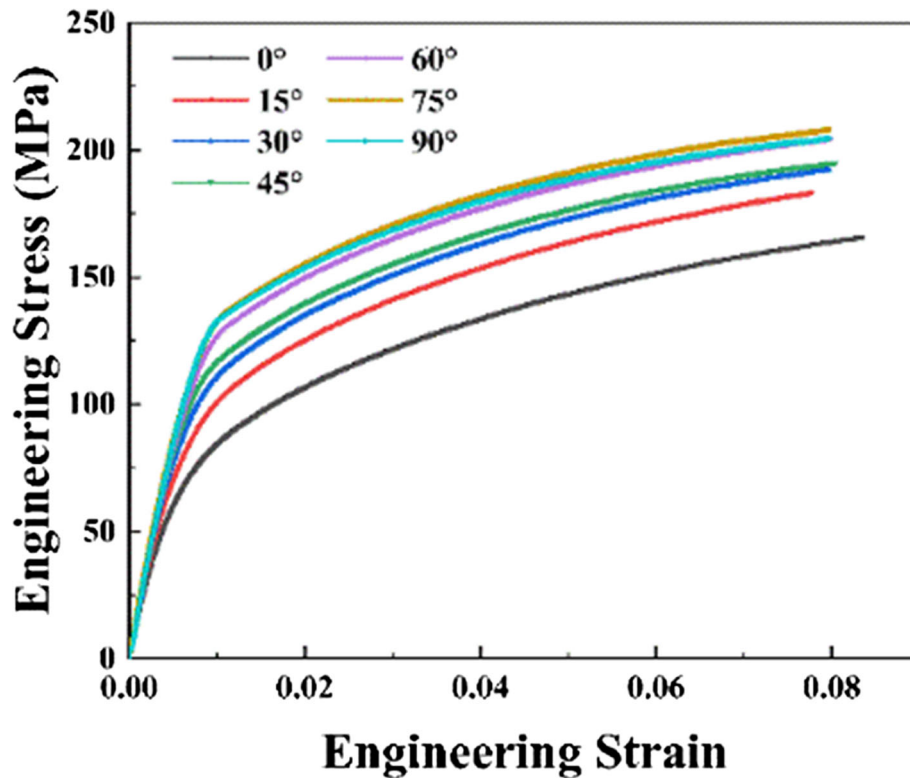
Fig. 1 Uniaxial tensile engineering stress-strain curve

activated at room temperature, specimens with higher basal slip activation have lower yield strengths (Ref 23). In this experiment, the mechanical properties anisotropy showed that the smaller the angle with TD, the higher the yield strength.

Figure 2 shows the microstructures of various specimens after tension in different directions at 6% strain. As can be seen from Fig. 2, all the tensile specimens exhibited homogeneous microstructures. The average grain sizes changed a little with the smallest of 10.8 μm in A15 sample and the largest of 14.7 μm in RD sample. The difference in grain size may be due to the difference in sample selection. The effect of grain size on corrosion behavior could be negligible. In addition, it can be found that almost no deformation twins in samples were observed.

3.2 Hydrogen Evolution Tests

3.2.1 NaCl Solution. In order to investigate the effect of tensile direction on corrosion rate, the different samples were immersed in 3.5 wt.% NaCl solution for 7 days (168h) and the volume of hydrogen precipitation is shown in Fig. 3. The hydrogen evolution curve shows a convex shape, which is caused by the formation of corrosion products and the dynamic

change of cracks (Ref 24). The corrosion rate decreased with increasing immersion time. Figure 4 shows the rates of hydrogen evolution (P_H) and weight loss (P_W) for tensile specimens in different orientations. As the angle with the RD direction increases, the P_H first decreased and then increased, and the corrosion rate of A45 specimen shows the smallest value of 2.1 mm/y. The P_W exhibits a similar trend.

The macro-morphology of the tensile specimens in different directions is shown in Fig. 5. The surfaces of all samples after immersion are rough and pitting. It is clear to see that the surface of the A45 specimen has the most uniform corrosion compared to other specimens. For samples A60, A75 and A90, a significant increase in the number of pitting could be clearly observed, and the range extended from the bottom to the upper part of the samples, where the A90 sample was the most obvious.

Figure 6 shows SEM images of AZ31 alloy after tension at strain of 6% and immersed in 3.5% wt.% NaCl solution for 7 days. Figure 7 displays the corresponding SEM cross sections for various samples. As shown in Fig. 6(a), (b) and (c), pitting corrosion pits were obviously observed in RD sample, and large and shallow corrosion marks were found in A15 sample. Compared with the RD and A15 samples, the A30 sample had
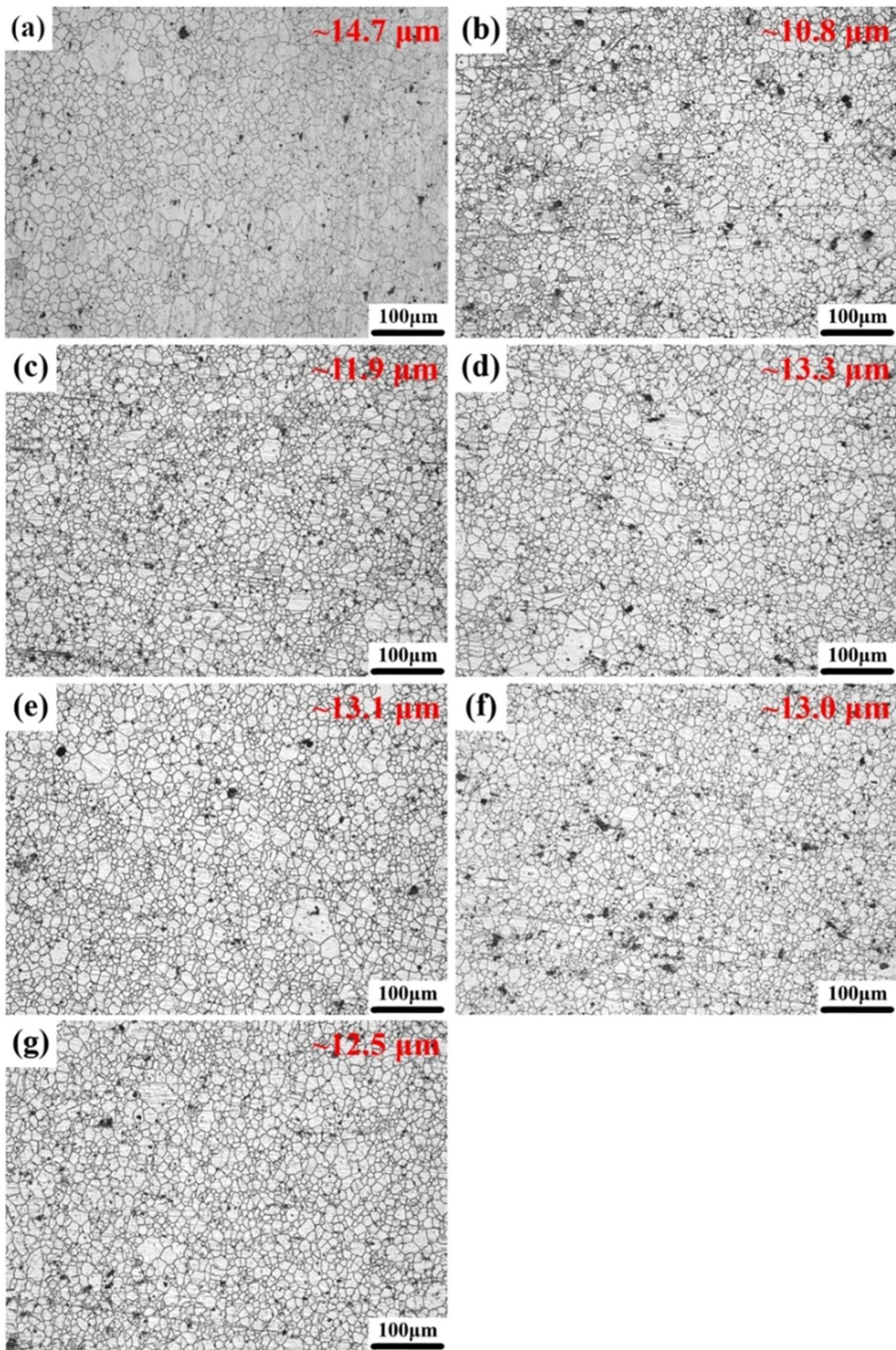
Fig. 2 Optical micrographs of Mg alloy AZ31 sheets (a) RD, (b) 15°, (c) 30°, (d) 45°, (e) 60°, (f) 75° and (g) 90°
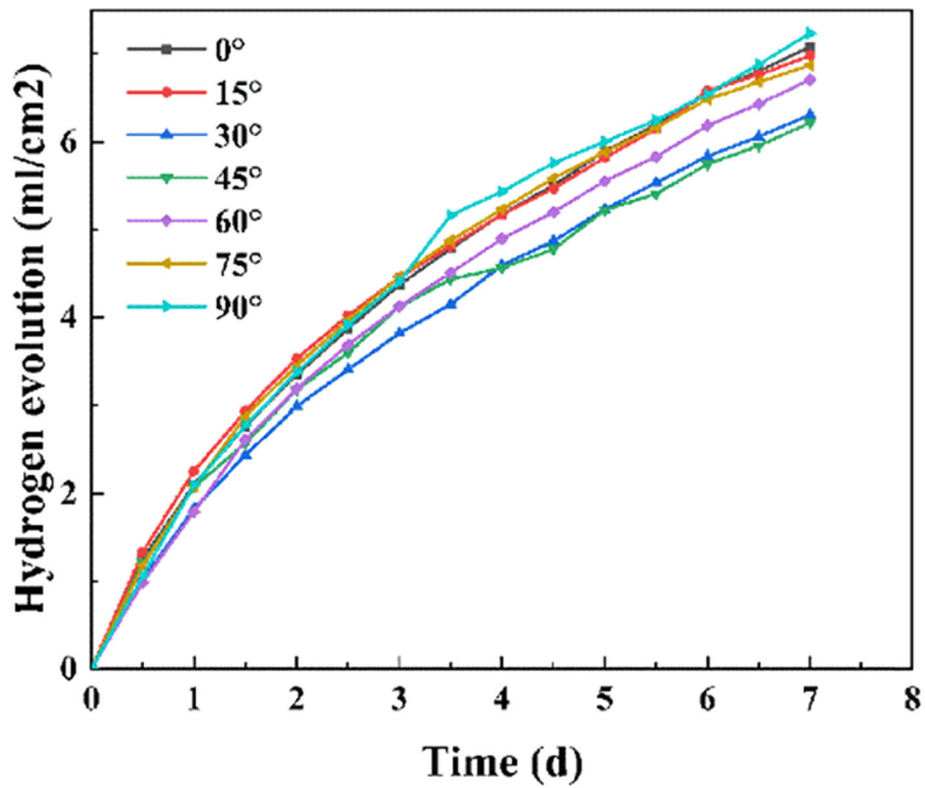
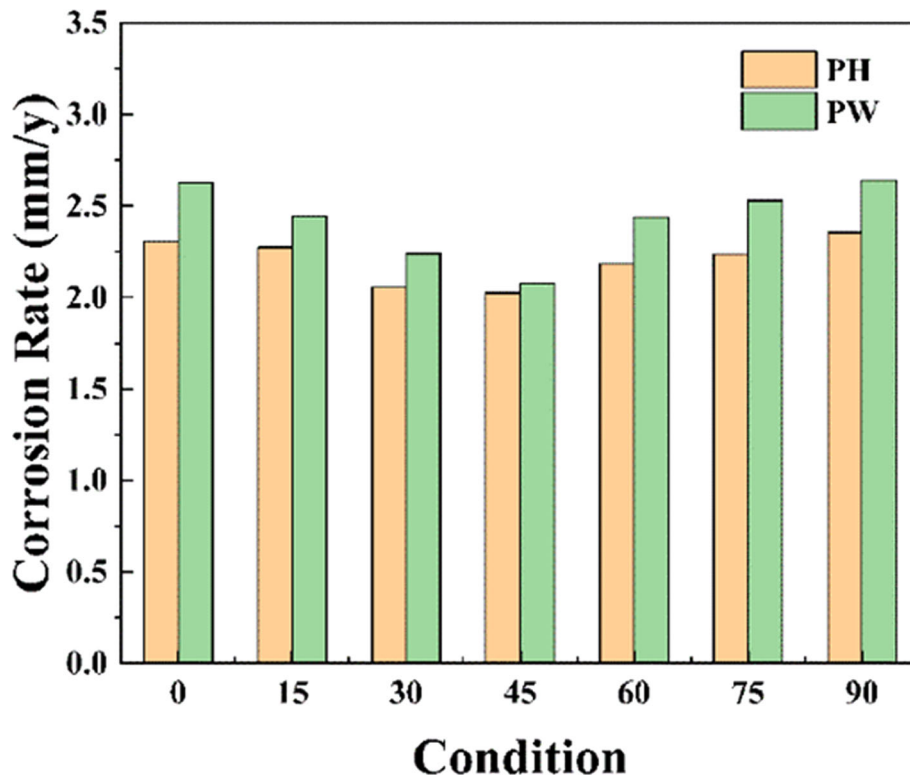**Fig. 3** Hydrogen evolution volume of AZ31 Mg alloy samples immersed in 3.5 wt.% NaCl solution for up to 7 days

Fig. 4 The average hydrogen evolution rate (P_H) and average weight loss rate (P_W) of the AZ31 Mg alloy sheet after 3.5 wt.% NaCl solution immersion for 7 days
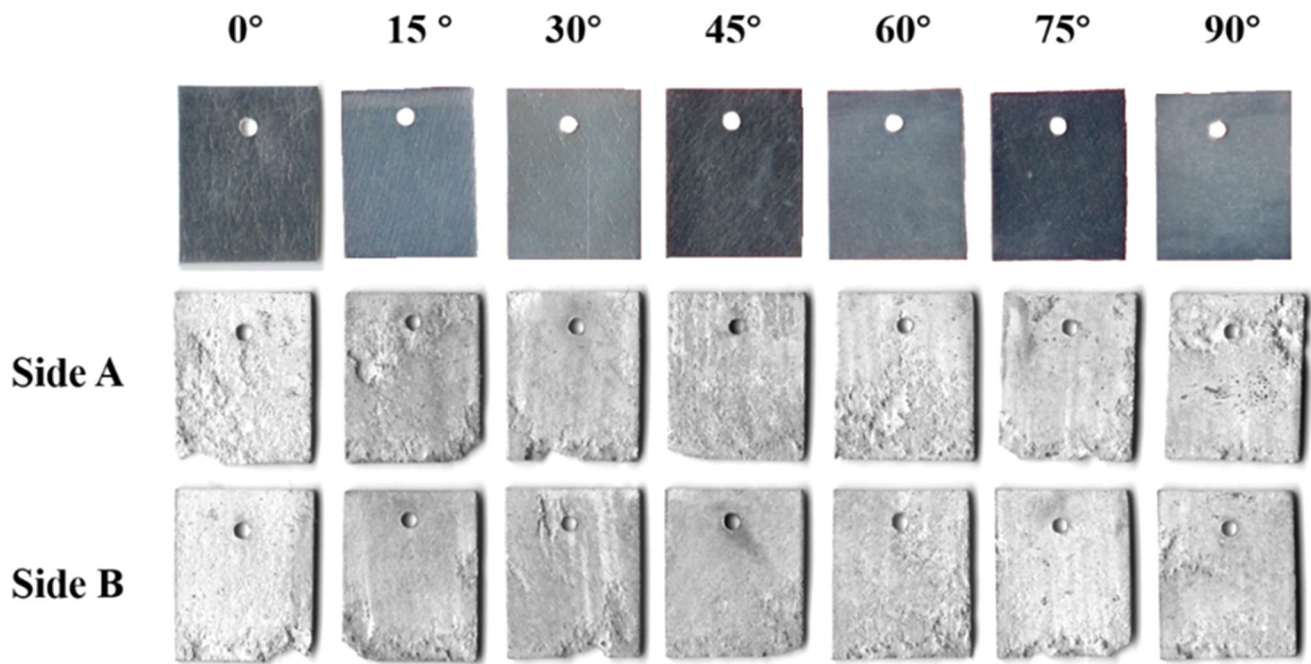
Fig. 5 Surface macro-morphology before and after immersion in 3.5 wt.% NaCl solution for 7 days

only a few pits that have been found and the size of the pitting area was smaller. From Fig. 7(a), (b) and (c), it can also be seen that the deepest depth of the corrosion pit reduced from 96.9 to 73.9 μm. The edges of the specimens are relatively clear with small gaps (Fig. 7a and b). The compact and uniform corrosion marks were obviously observed in A45 sample. The edges are sharp and clear without notches, as shown in Fig. 7(d). The depth of corrosion pits is only 26.3 μm, the smallest among all samples. According to Fig. 6(e), (f) and (g), it could be found that pitting corrosion appeared and gradually increased with the angle; especially in Fig. 6(g), continuous corrosion pits appeared on the surface. In comparison, there are only a small number of corrosion pits on the A75 sample with the most complete edge of the sample, but the depth of the corrosion pit is deeper than the other specimen. According to Fig. 7(f), the side edges are more complete than the samples tensioned in RD. And the range of etch pit depth is 70.6 μm. It means that the anisotropy of the material leads to differences in the corrosion behavior of the material (Ref 25). That is, as the angle with the RD increases, the sharp edges gradually disappeared. And the depth of the corrosion pits gradually increased and the width became wider. The difference of tensile direction has great influence on the corrosion behavior of the samples. The results show that the corrosion rate of the material could be determined by the texture of the material at approximate residual stress levels, but to a limited extent. Compared with the experimental group of different tensile directions, it can be

found that the dislocation entanglement and twinning have enhanced the corrosion resistances (Ref 26).

3.2.2 Na$_2$SO$_4$ Solution. Figure 8 shows the immersion hydrogen evolution data of 6% magnesium alloy sheet tensioned in different directions. The immersion period is 7 days, the same as in the NaCl solution. The fastest hydrogen precipitation rates were obtained in the first 3 days. The total amount of hydrogen evolved increased as the immersion time increases. However, the rate of hydrogen evolution decreased due to the formation of the corrosion product film. Figure 9 displays the hydrogen evolution rate (P_H) and weight loss rate (P_W), showing the same tendency of corrosion rate in NaCl solution, decreasing and then increasing as the angle with RD increases. The corrosion resistance is greatest when the angle with RD is 45°. The hydrogen evolution and weight loss rates of the samples under various conditions in the Na$_2$SO$_4$ solution are lower than those in the NaCl solution. As mentioned before, compared to NaCl solution, different tensile samples had higher corrosion resistance in Na$_2$SO$_4$ solution.

The macro-morphology before and after immersion is shown in Fig. 10. Compared with the samples before immersion, the metallic luster of the samples became weaker, and the local corrosion appeared. Different from the evenly distributed pitting corrosion on the sample surface in NaCl solution, a large range of corrosion pits only appeared at the edge of the sample in Na$_2$SO$_4$ solution, while the corrosion in other areas was very slight, and it also retained part of the metallic luster before corrosion.
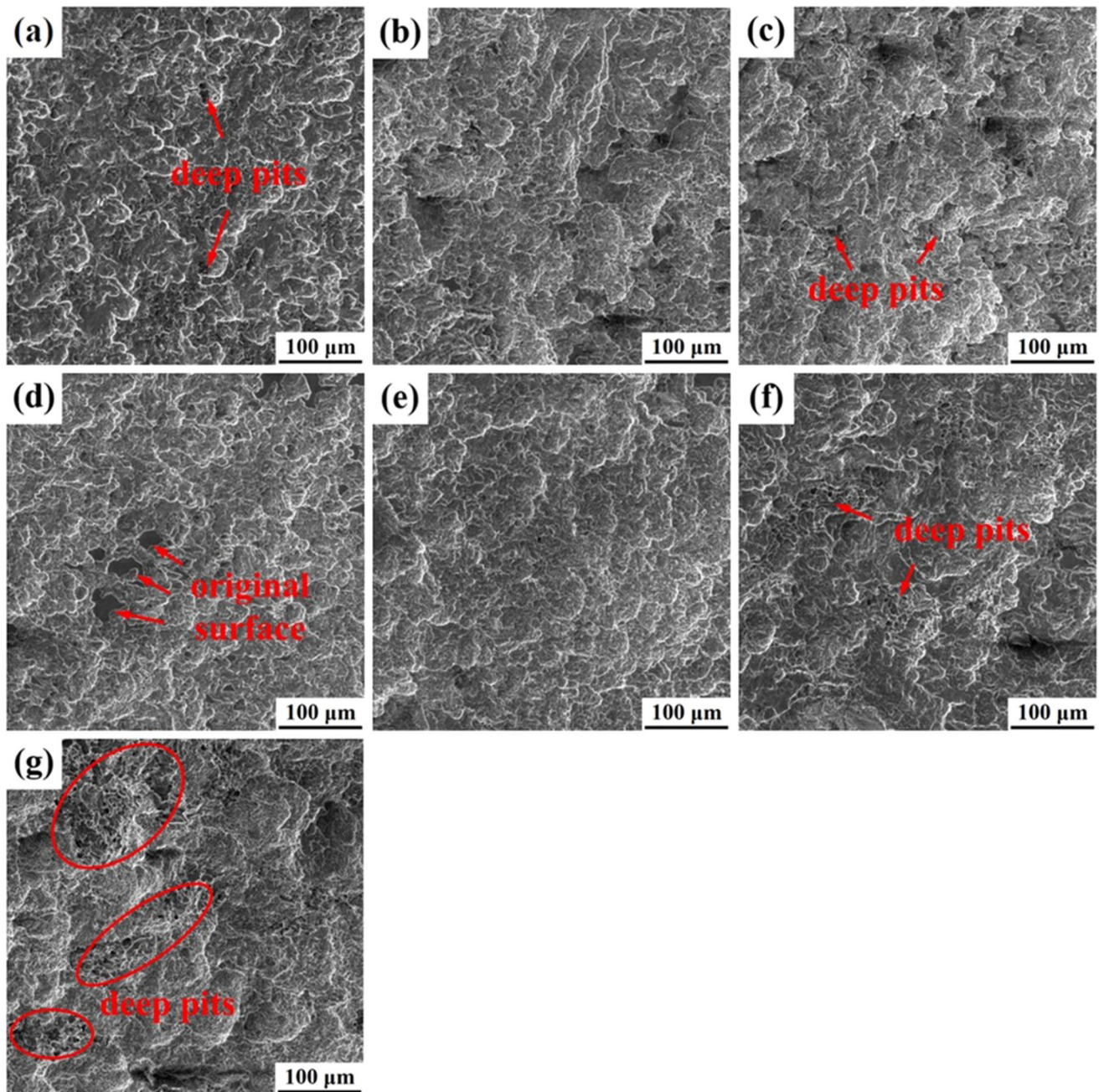
Fig. 6 SEM micrographs of the samples after immersion in 3.5 wt.% NaCl solution for 7 days: (a) RD, (b) 15°, (c) 30°, (d) 45°, (e) 60°, (f) 75° and (g) 90°

Figure 11 displays the SEM image of the surface of the specimen after immersion and the corresponding SEM cross section is shown in Fig. 12. It could be obviously found that the local corrosion depressions with a diameter of 20-50 μm in the specimens of the RD and the cross section had a gentle erosion slope. As shown in Fig. 11(b) and (c), the shape of the corrosion pits gradually became blurred, forming a continuous and uniform corrosion surface. From Fig. 12, it can be seen that there were slight corrosion marks on the edges of the cross section with the depths of 62.2 and 23.8 μm, respectively. As shown in Fig. 11(d), the A45 sample shows no obvious corrosion pits and the edges of the cross section are clear and
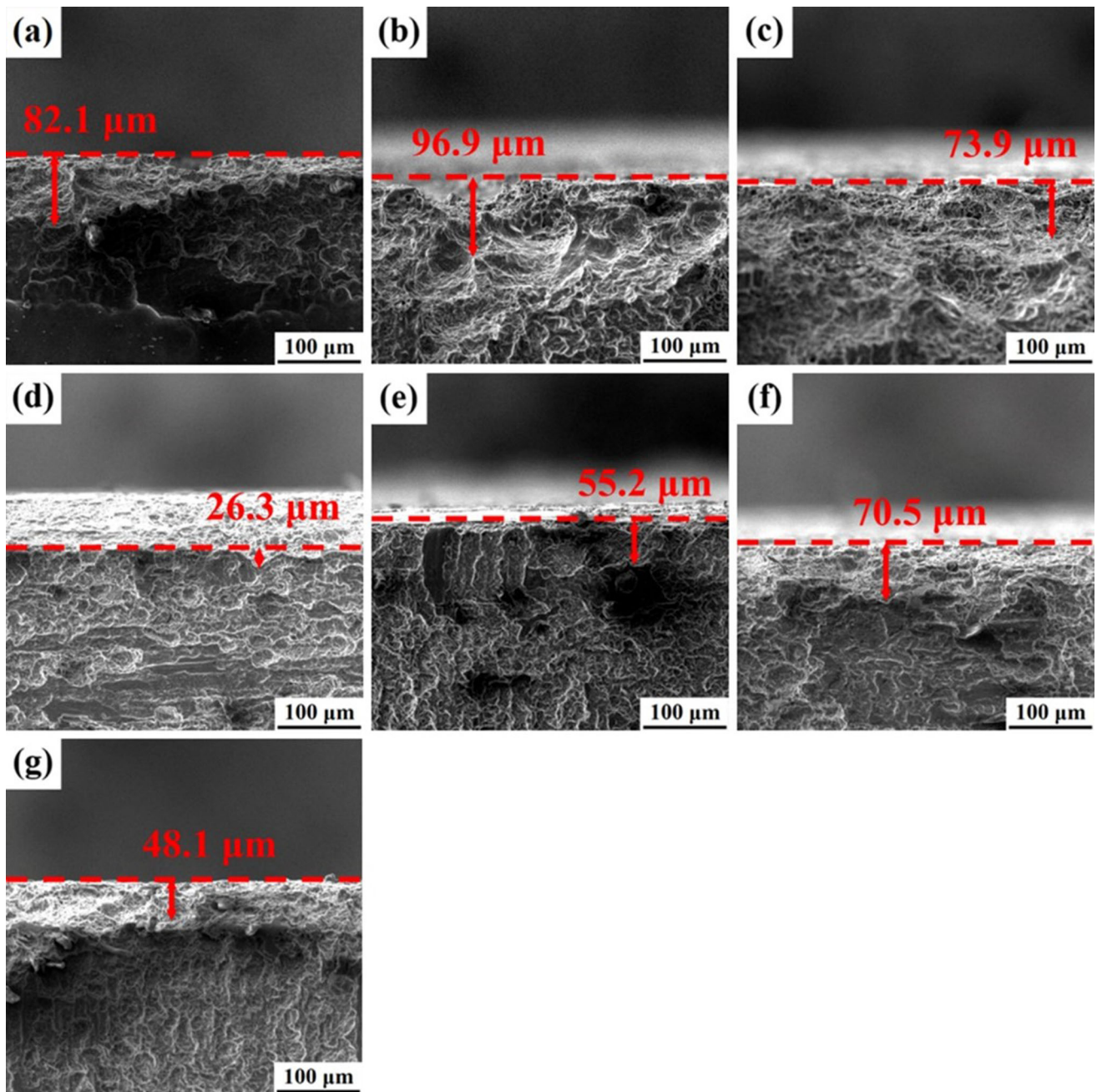
Fig. 7 Cross section SEM micrographs of the samples after immersion in 3.5 wt.% NaCl solution for 7 days: (a) RD, (b) 15°, (c) 30°, (d) 45°, (e) 60°, (f) 75° and (g) 90°

complete. When the angle between the tensile direction and RD exceeded 45°, corrosion pits gradually appeared on the surface of the sample and gradually developed from uniform and slight corrosion to large and shallow corrosion pits, resulting in large corrosion pits (Fig. 11g). In Fig. 12(e), (f) and (g), it shows an increase in the depth of corrosion pits.

Local corrosion pits could be found in Fig. 12, with the interface edges of the sample intact and smooth. The surface corrosion SEM image did not find the tunnel pitting pits with a diameter less than 5 μm. Compared with the corrosion pits of tens to hundreds of microns, it should be called corrode depressions. The SEM image is mutually corroborated with the
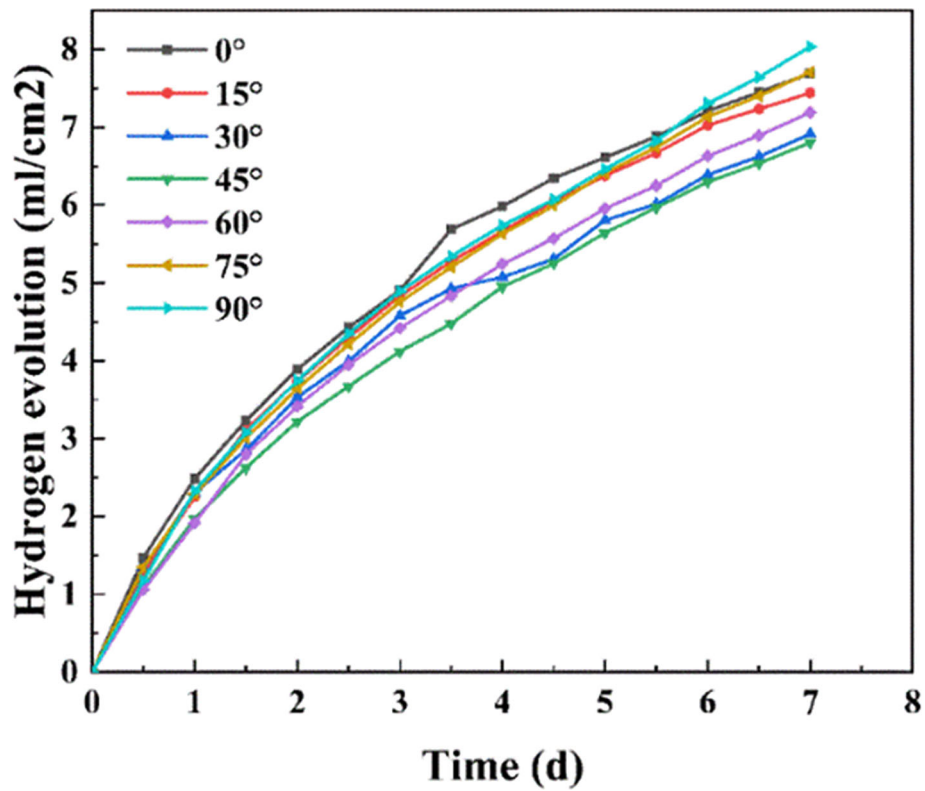
Fig. 8 Hydrogen evolution volume of AZ31 Mg alloy samples immersed in 8.5 wt.% Na_2SO_4 solution for 7 days
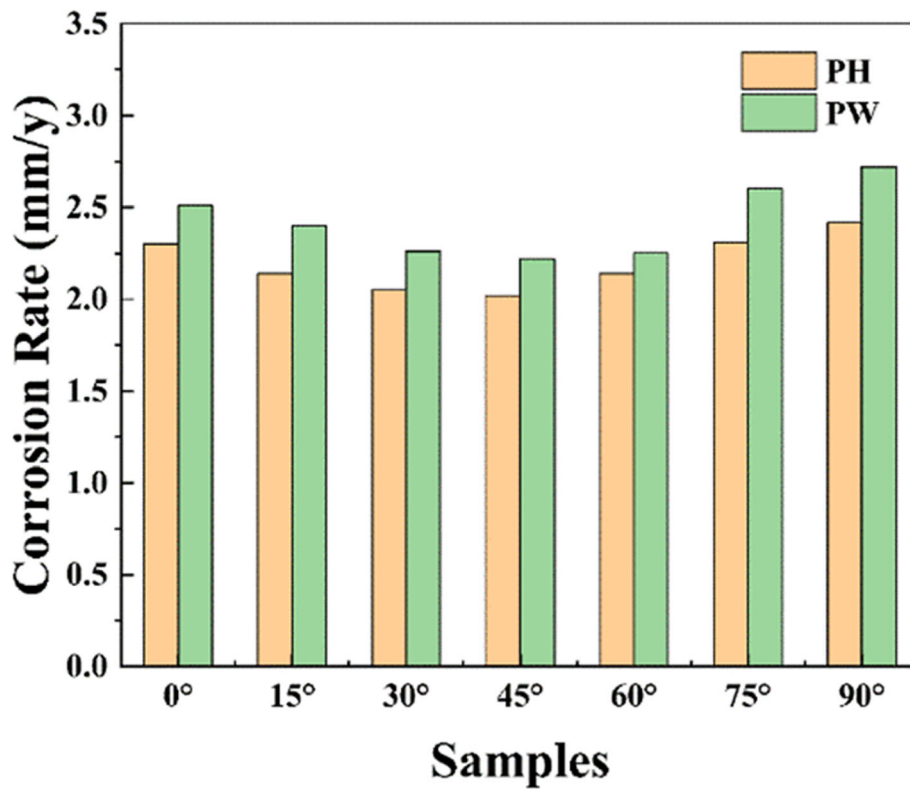

Fig. 9 The average hydrogen evolution rate (PH) and average weight loss rate (PW) of the AZ31 Mg alloy sheet after 8.5 wt.% Na_2SO_4 solution immersion for 7 days
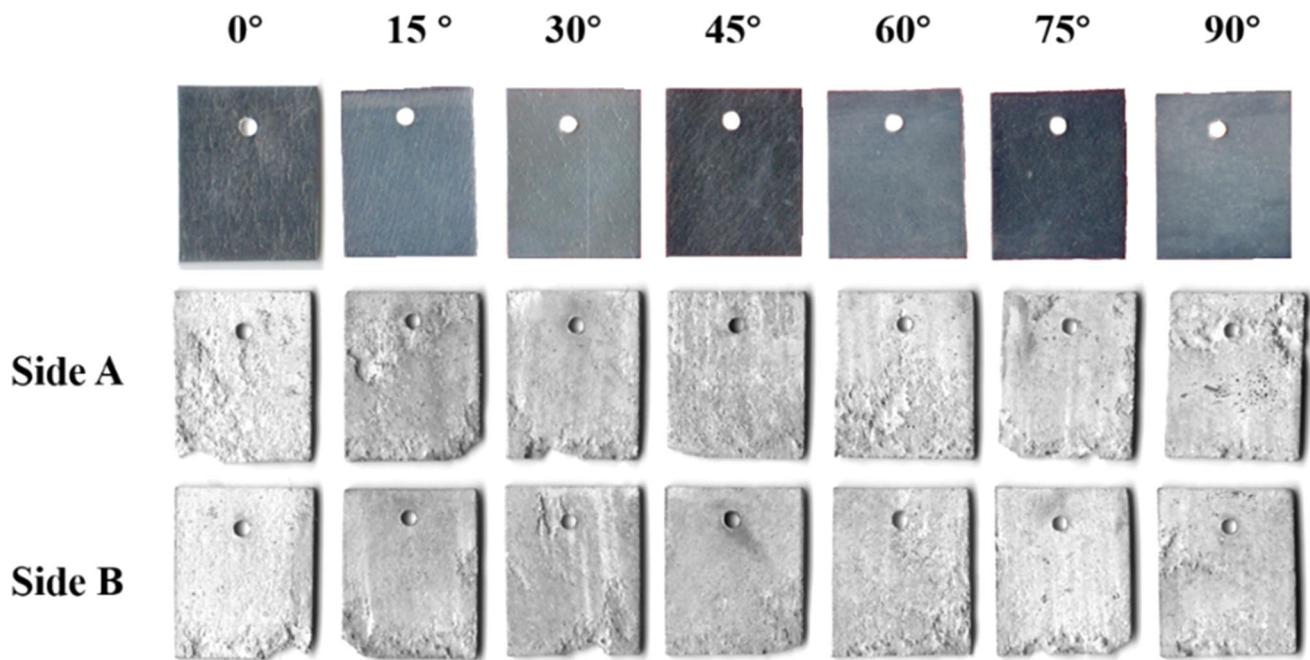
Fig. 10 Surface macro-morphology before and after immersion in 8.5 wt.% Na$_2$SO$_4$ solution for 7 days

rate of hydrogen evolution and weightlessness corrosion, indicating that the effect of tensile direction on the corrosion performance of AZ31 magnesium alloy sheets in Na$_2$SO$_4$ solution was the same as that in NaCl solution. The corrosion rate increases with the angle between the tensile direction and RD, and the best corrosion resistance is achieved at 45°. However, under the same conditions, the corrosion performance of the sample in Na$_2$SO$_4$ solution is more uniform and the corrosion resistance is higher, which may relate to the stronger protective effect of the corrosion product film in Na$_2$SO$_4$ solution.

3.3 Electrochemical Testing

3.3.1 NaCl Solution. The open-circuit potential curves of different tensile directions samples in 3.5 wt.%NaCl solution are shown in Fig. 13. After 1000 s, the potential of the samples gradually stabilized. Figure 14 shows the electrochemical impedance spectrum (EIS) and the equivalent circuit model. The treated sample showed capacitive loops at all frequencies and inductive regions at lower frequencies. A45 sample exhibits the largest impedance comparing to the other specimens, indicating the best corrosion resistance. It could be also found in Fig. 14(c), A45 samples had the highest impedance among the alloys (Ref 27). In Fig. 14(b), the wider and larger phase angle of A45 becomes in the intermediate frequency range, indicating the greater protection of oxide film formed on

the substrate. As for the Bode plot of phase angle frequency, all samples have a crest and a trough, corresponding to the presence of a capacitive loop and an inductive loop in Fig. 14(a) (Ref 28). The EIS fitting results of samples in different directions are shown in Table 1. R_s and R_{ct} represented the solution resistance and charge transfer resistance, respectively. CPE is the constant phase element. Capacitive circuits are created by the formation of oxide films on the substrate due to the capacitive charge transfer of the electric double layer, characterized by R_{ct} and CPE_{dl}. The adsorption of corrosion products leads to the appearance of inductive loops, which is characterized by R_L and L (Ref 29). The R_{ct} value increased and then decreased as the angle between the tensile direction and the RD direction increases, reaching a maximum in the A45 specimen. R_{ct} is positively correlated with corrosion resistance, and the decrease in impedance is reflected by the increase in Q_{dl} and the decrease in the value of the entire induction loop. The variation in the components proves that the corrosion resistance is consistent with the results of the immersion test.

Figure 15 shows the dynamic polarization curves of the AZ31 magnesium alloy specimens in different tensile directions. It can be found that all samples have a passivation zone. This indicated that a thin oxide layer was formed on the substrate, covering the active area, and the continuous passivation would lead to the formation of a dense phase-forming layer on the surface. The data of E_{corr} and i_{corr} obtained by cathode extrapolation method are shown in Table 2. A45
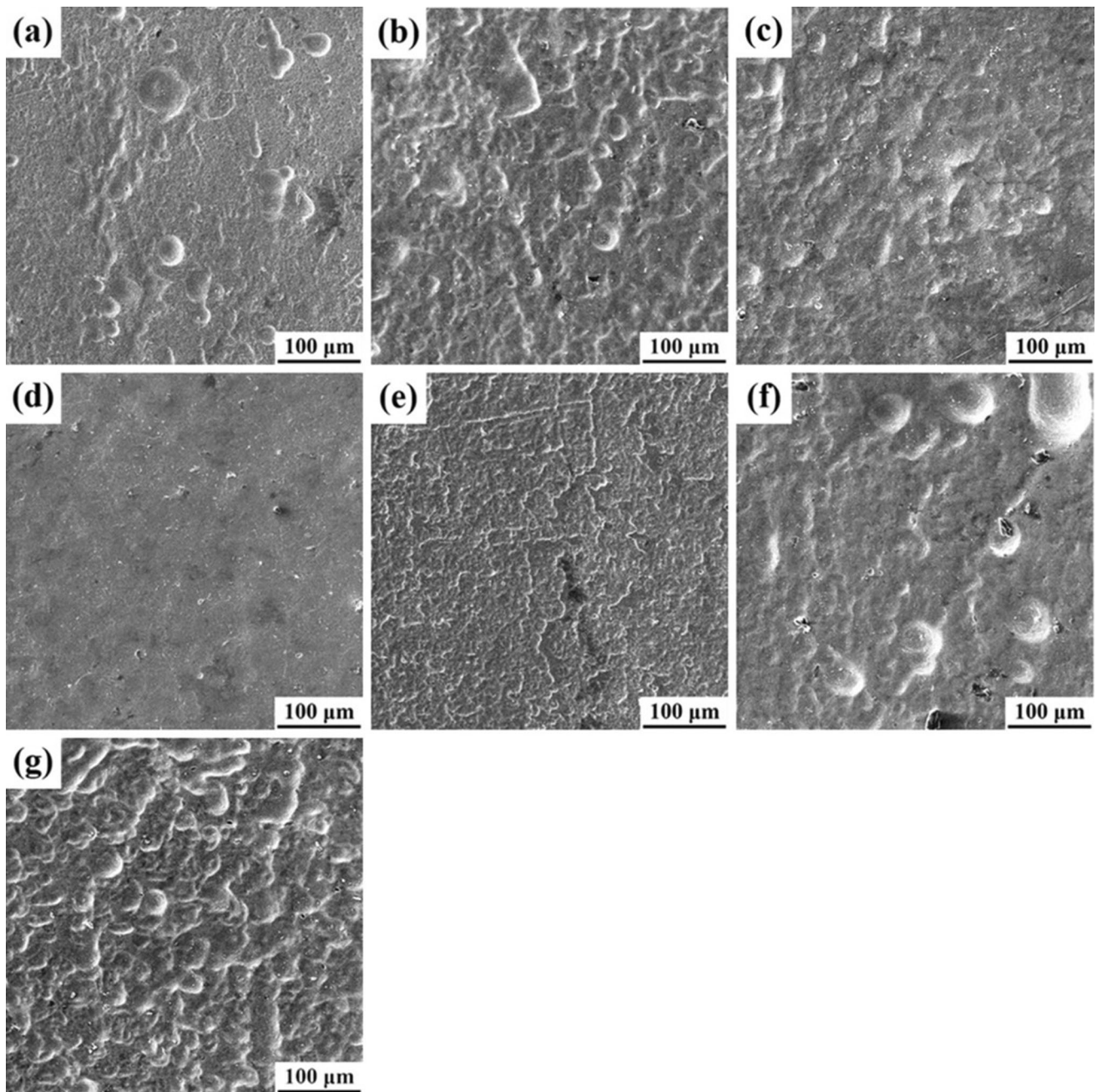
Fig. 11 SEM micrographs of the samples after immersion in 8.5 wt.% Na$_2$SO$_4$ solution for 7 days: (a) RD, (b) 15°, (c) 30°, (d) 45°, (e) 60°, (f) 75° and (g) 90°

specimen has the lowest corrosion current, 2.91 μA cm^{-2}. It could be found that the further the angle of the specimen deviates from 45° direction, the higher the value of i_{corr}. The corrosion resistance increases and then decreases with the angle to the RD direction, reaching a maximum at 45°, in line with the mechanical properties. According to the previous research, the 45° direction made the substrate have the highest elongation (Ref 30). Studies have also shown that the strain hardening index in the direction of 45° was slightly smaller than that of 0 and 90° (Ref 31). This indicated that the 45° direction was less prone to dislocation accumulation during plastic deformation, leading to a better coordinated deformation performance. As the dislocation accumulation mentioned above impairs the corrosion resistance, the A45 sample had the best corrosion resistance, which was consistent with the results of immersion test, microscopic morphology and AC impedance spectroscopy.
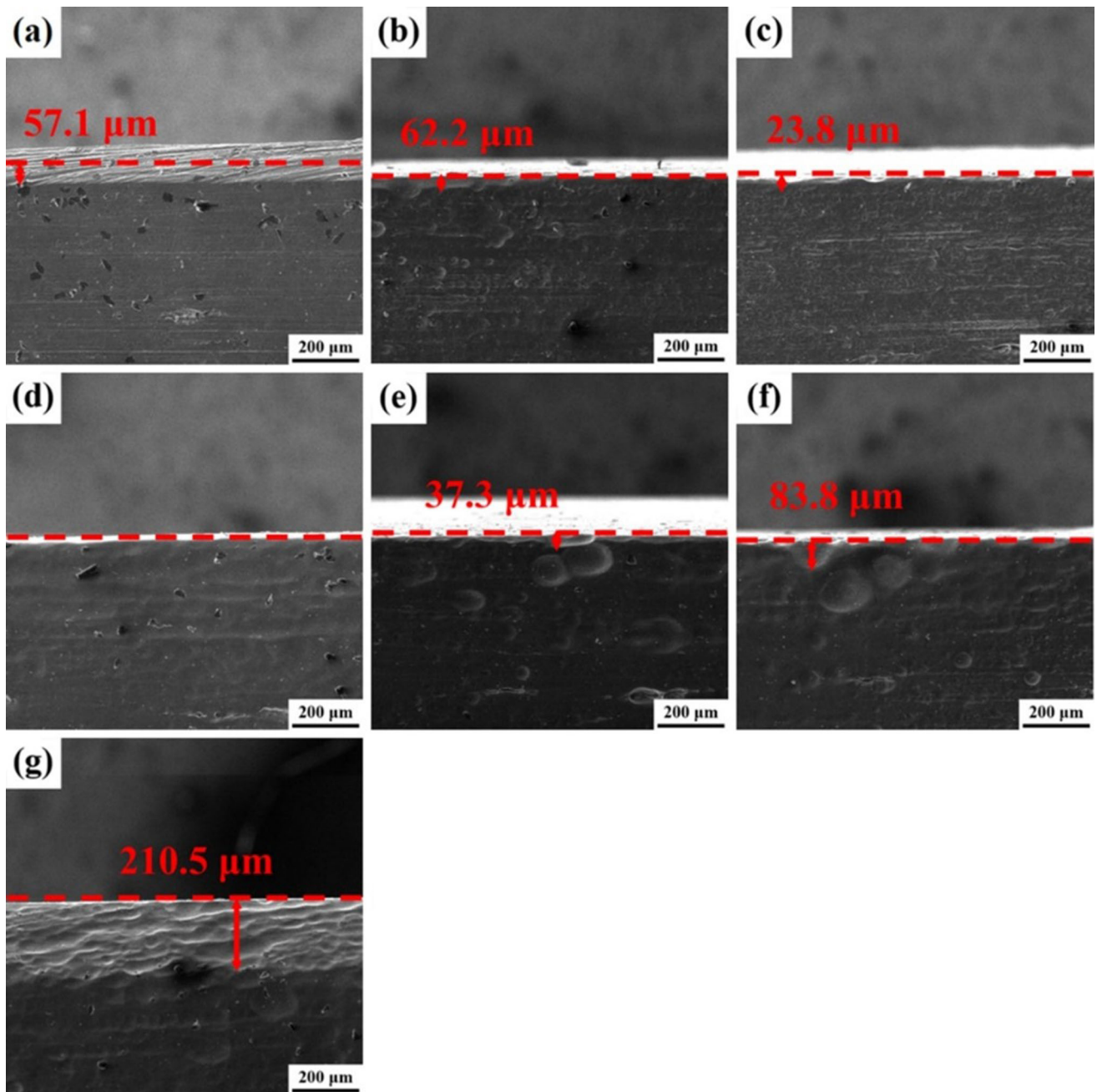
Fig. 12 Cross section SEM micrographs of the samples after immersion in 8.5 wt.% Na_2SO_4 solution for 7 days: (a) RD, (b) 15°, (c) 30°, (d) 45°, (e) 60°, (f) 75° and (g) 90°

Figure 16 shows the relationship between polarization resistance (R_p) or corrosion current and strain. With the increase of the angle with the RD direction, the corrosion current first decreased and then increased, reaching the lowest in the 45° direction. The results show that the electrochemical impedance spectra are corresponding to the kinetic potential polarization curves.

3.3.2 Na_2SO_4 Solution. Figure 17 shows the open-circuit potential curves for AZ31 magnesium alloy rolled sheet in 8.5 wt.% Na_2SO_4 solution. Over the obvious rise in the first 400 s, the maximum rise is approximately to 0.1 V, It is a process from the beginning of corrosion to dynamic stability (Ref 32). The process is longer than the unstable zone of 200 s in the NaCl solution, which indicates that the NaCl solution is more corrosive to the magnesium alloy matrix, produces an oxide film faster and reaches a dynamic stable state of corrosion
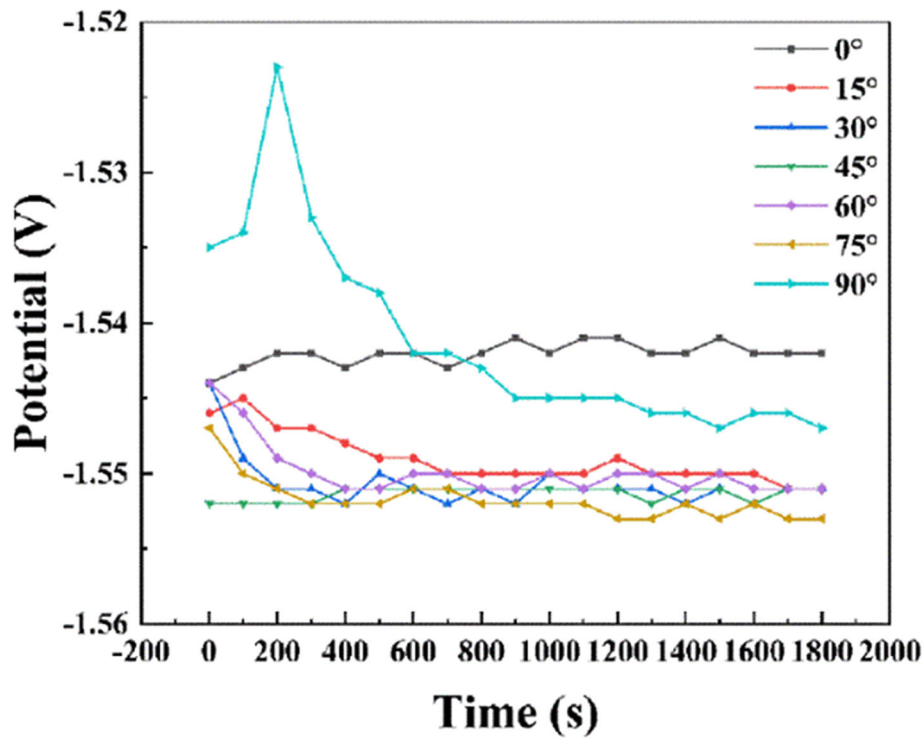
Fig. 13 OCP curves of the AZ31 Mg alloy samples in 3.5 wt.% NaCl solution for 0.5 h

(Ref 33).

Figure 18 shows the EIS and equivalent circuit model of the samples in 8.5 wt.% Na$_2$SO$_4$ solution. At the high frequency (Fig. 18a), capacitive reactance arcs could be found, while a diffusion curve could be found at low frequencies. A tendency of capacitive reactance was shown in the low-frequency region of the A30 sample, which was caused by the outward diffusion of dissolved magnesium ions in the corrosion product film (Ref 34). The law of capacitive reactance arc is that with the increase of the angle between the tensile direction and the RD direction, the impedance first increased and then decreased. The A45 sample has the largest impedance and the best corrosion resistance. This is the same as in the NaCl solution. However, the impedance arc in the Na$_2$SO$_4$ solution is significantly larger, that is, the corrosion ability of the Na$_2$SO$_4$ solution to the AZ31 magnesium alloy is weaker than that of the NaCl solution (Ref 35). A significant difference in the slope of the diffusion curve could be found in the low-frequency region. The slope of the sample along the RD direction is $\pi/4$. However, the samples in other directions are slightly smaller than $\pi/4$, which indicates that the tensile direction has an influence on the performance of the magnesium alloy corrosion product film.

For all the samples, the AC impedance diagram could be described by the equivalent circuit shown in Fig. 18(d), where R_s is solution resistance; CPE_{dl} and R_{ct} are the electric double-layer capacitance and the charge transfer resistance between the material surface and the solution interface, respectively. W is the Weber impedance (representing the impedance during diffusion) (Ref 36). The results of the EIS fitting for the different strained samples are shown in Table 3. The equivalent circuit impedance value calculation formula is shown in Eq 2. The solution resistance (R_s) is similar. The R_{ct} value increases and then decreases as the angle between the stretching direction and the RD direction increases, which attained the maximum value 3588 $\Omega \cdot cm^2$ at the A45 sample. According to Eq 3, the A45 sample has higher corrosion resistance. The change rule of W was opposite to R_{ct}, and the A45 sample was the lowest. This rule is the same as the previous immersion corrosion.

$$Z = R_s + \frac{1}{Q_{dl}(j\omega)^n + \frac{1}{R_{ct}}} + Z_W \qquad \text{(Eq 3)}$$

Figure 19 shows the polarization curves for all samples in 8.5 wt.% Na$_2$SO$_4$ solution. Due to the linear region of the cathodic polarization curve, I_{corr} was obtained using the Tafel
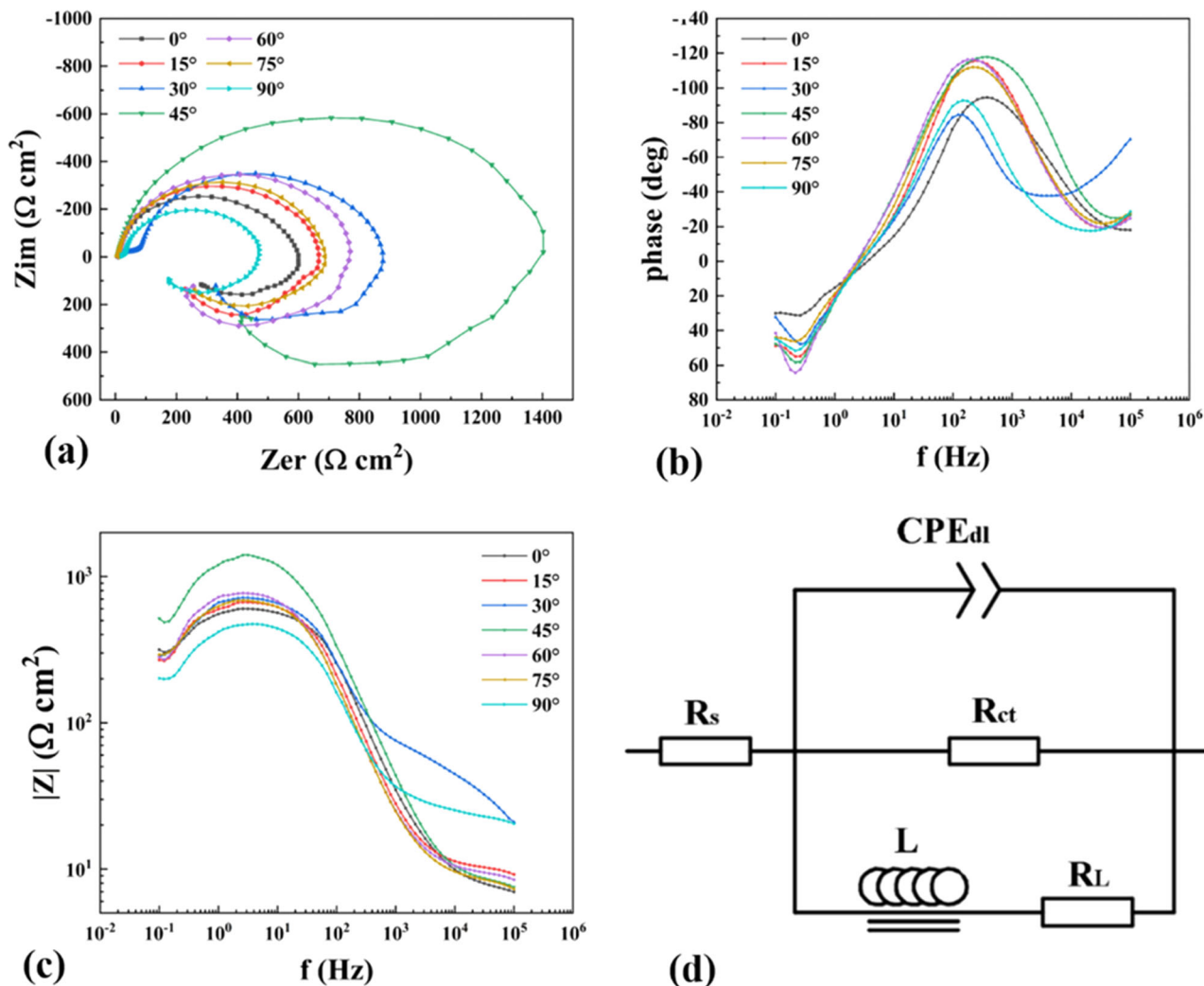
Fig. 14 Electrochemical impedance spectra and equivalent circuit models: (a) Nyquist plots, (b) Bode plots of phase angle (θ) vs. f, (c) Bode plots of |Z| vs. f and (d) Equivalent circuit models used for fitting the impedance spectra in (a)

Table 1 Fitting results of the EIS for the samples with different strains

Sample	R_s, Ω cm^2	Q_{dl}, $\mu\Omega^{-1}$ s^{-n} cm^{-2}	n_{dl}	R_{ct}, Ω cm^2	L/H cm^2	R_L, Ω cm^2
RD	7.572	10.7	0.8997	594.6	391.0	413.0
A15	10.21	11.07	0.9324	657.9	356.9	245
A30	10.12	9.688	0.8998	808.9	357.8	314.3
A45	7.949	8.442	0.9048	1381	594.9	471.1
A60	9.42	15.01	0.9111	782.7	360.9	250.2
A75	8.367	14.57	0.9129	689.5	367.7	314.8
A90	24.02	21.48	0.8746	460.3	208.7	172.2

extrapolation method. The related values are shown in Table 4, including i_{corr} and E_{corr}. The value of self-corrosion potential is relatively close. The farther the tensile deformation direction deviates from 45°, the higher the self-corrosion current, which is consistent with the performance in NaCl. It indicates that Cl⁻

and SO$_4^{2-}$ have the same effect on dislocation stacking and stress concentration caused by different stretching directions (Ref 37). However, the i_{corr} in Na$_2$SO$_4$ was a slightly higher, compared to the value in NaCl. It was caused by the difference in volume of Cl⁻. For Cl⁻, twinning facilitates the invasion of

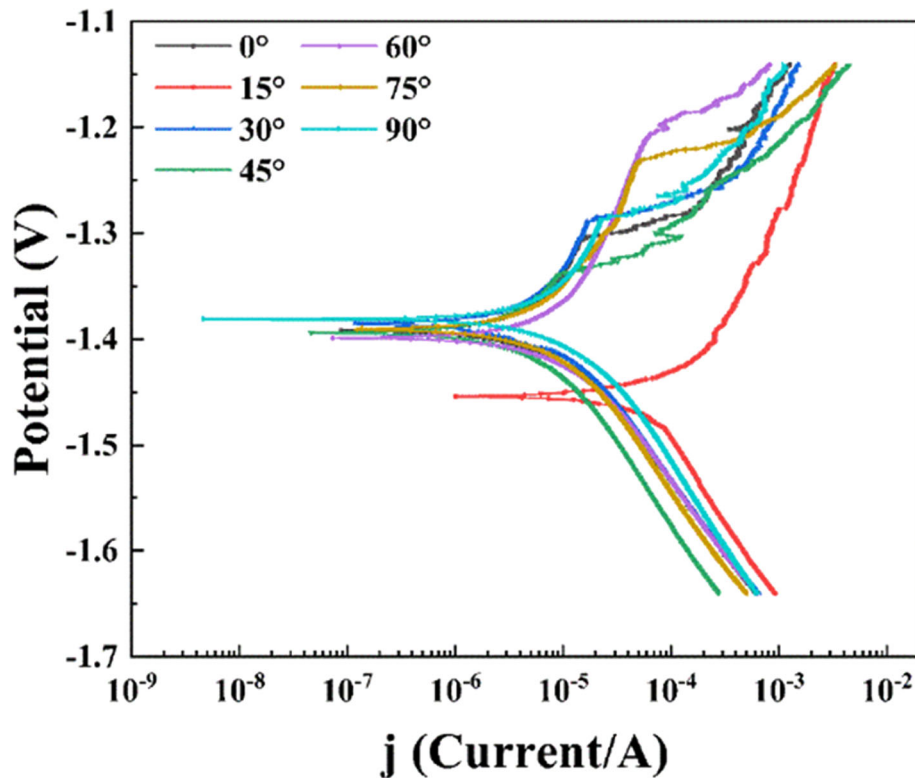**Fig. 15** Potentiodynamic polarization curves of samples measured in 3.5 wt.% NaCl solution after 0.5 h stabilization

Table 2 Fitting results of polarization curves for samples with different strains

Tensile direction	0°	15°	30°	45°	60°	75°	90°
i_{corr}, $\mu A\ cm^{-2}$	4.69	18.23	3.82	2.91	4.52	4.14	5.99
E_{corr}, $V_{Ag/AgCl}$	− 1.392	− 1.454	− 1.385	− 1.394	− 1.399	− 1.391	− 1.381

the magnesium matrix and promoted the dissolution of magnesium. On the contrary, twinning hinders electron migration and inhibits the diffusion of pitting corrosion for SO_4^{2-}.

4. Conclusion

(1) The average grain sizes of AZ31 rolled sheets were not significantly affected by the different tensile directions, which was ranged from 10.8 to 14.7 μm

(2) The influence of corrosive media on AZ31 magnesium alloy was very significant. For magnesium alloys, the substrate texture has strong corrosion resistance. The in-crease of stress variable will enhance the strength of the substrate surface and reduce the corrosion rate of the sample. The difference from the NaCl solution is that the volume of SO_4^{2-} is larger, and $MgSO_4$ has a lower solubility than $MgCl_2$, so the corrosion product film containing MgSO4 will be less prone to rupture and has a stronger protective effect (Fig. 20).

(3) The tensile directions influent the corrosion behavior of the specimens significantly. The corrosion rate first decreased with the increase of the angle between RD and then increased, which attained the minimum of 2.1 mm/y in A45 specimen. The similar trend was obtained in electrochemical testing, such as in EIS and potentiodynamic polarization curves. The results indicated that the A45 sample had the highest corrosion resistance.
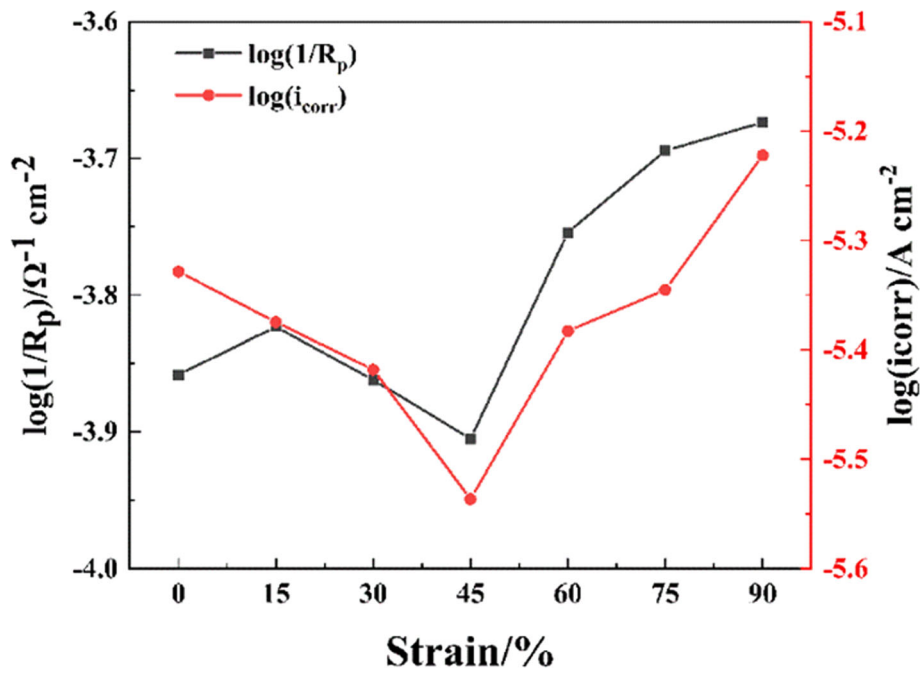
Fig. 16 Corrosion rate ($1/R_p$) and corrosion current (i_{corr}) as a function of strain for AZ31 magnesium alloy
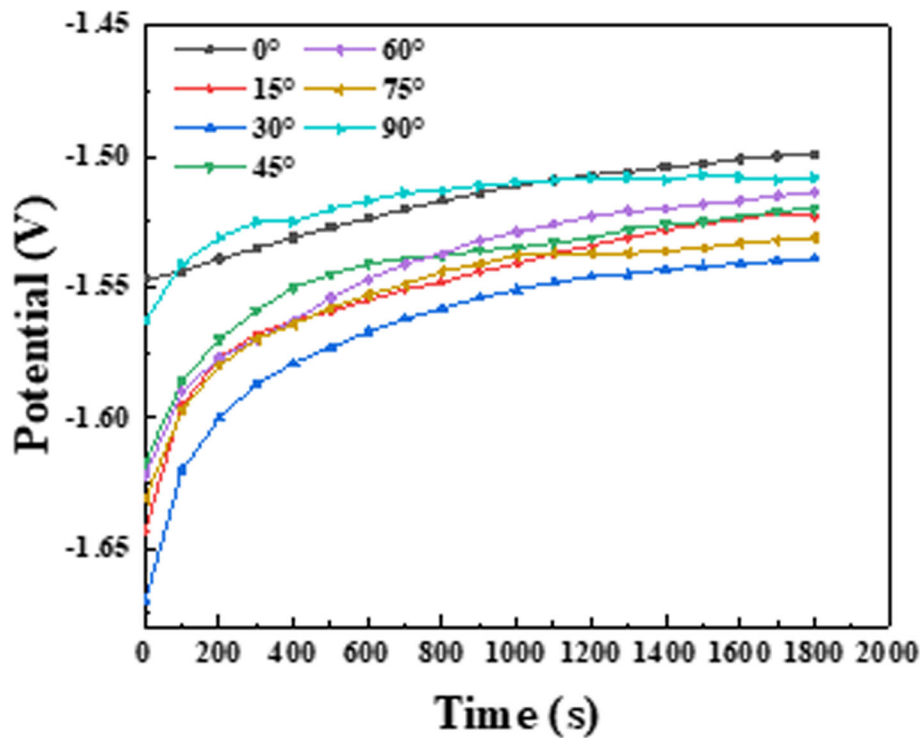

Fig. 17 OCP curves of the AZ31 Mg alloy samples in 8.5 wt.% Na_2SO_4 solution for 0.5 h
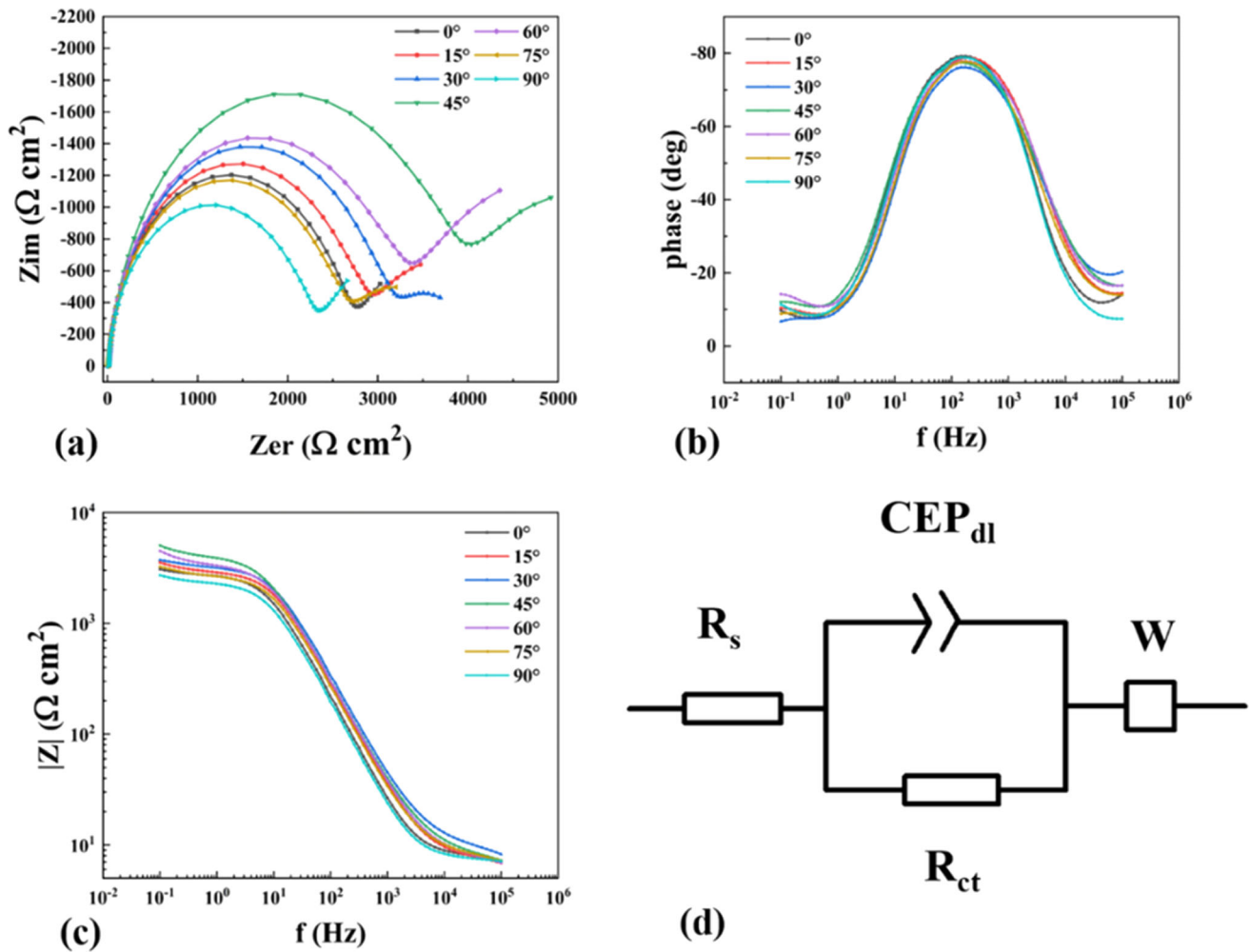
Fig. 18 Electrochemical impedance spectra and equivalent circuit models: (a) Nyquist plots, (b) Bode plots of phase angle (θ) vs. f, (c) Bode plots of |Z| vs. f and (d) Equivalent circuit models used for fitting the impedance spectra in (a)

Table 3 Fitting results of the EIS for the samples with different strains

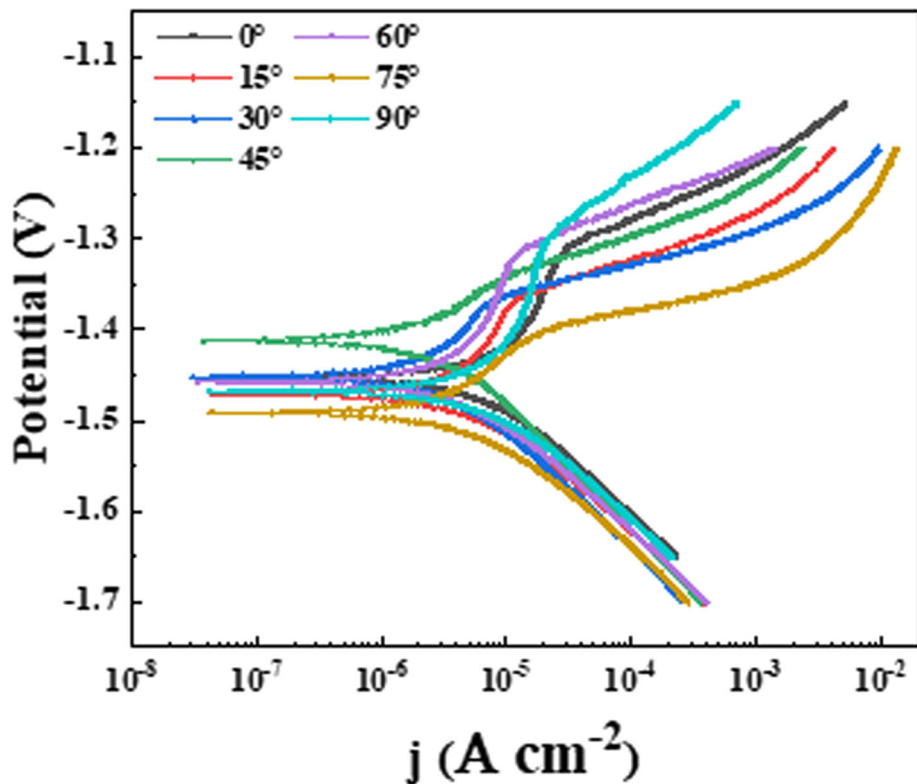| Sample	R_s, Ω cm^2	Q_{dl}, $\mu\Omega^{-1}$ s^{-n} cm^{-2}	n_{dl}	R_{ct}, Ω cm^2	W, $\mu\Omega^{-1}$ s^{-n} cm^{-2}
RD	7.001	9.259	0.9749	2546	2496
A15	6.297	7.02	0.9762	2659	1467
A30	7.765	6.937	0.9542	2851	1051
A45	6.274	7.365	0.9688	3588	937.6
A60	5.983	6.964	0.9781	3034	1039
A75	6.782	7.973	0.9696	2435	1480
A90	6.776	10.54	0.9717	2188	3017

Fig. 19 Potentiodynamic polarization curves of samples measured in 8.5 wt.% Na_2SO_4 solution after 0.5 h stabilization

Table 4 Fitting results of polarization curves for samples with different strains

Tensile direction	0°	15°	30°	45°	60°	75°	90°
i_{corr}, μA cm^{-2}	5.96	5.82	3.73	3.29	4.72	6.54	7.54
E_{corr}, $V_{Ag/AgCl}$	− 1.449	− 1.471	− 1.452	− 1.412	− 1.458	− 1.491	− 1.468

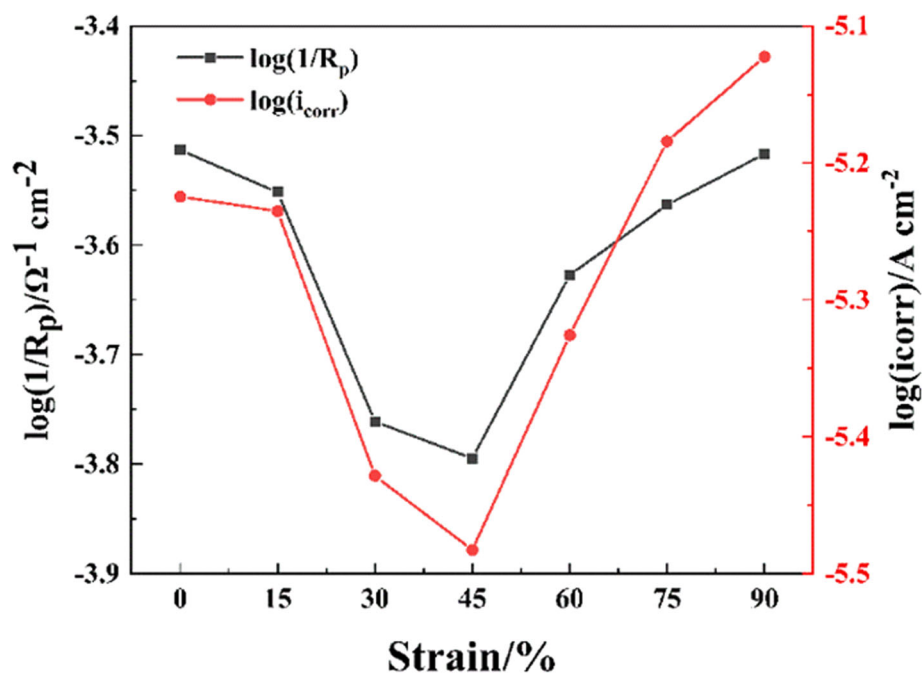**Fig. 20** Corrosion rate ($1/R_p$) and corrosion current (i_{corr}) as a function of strain for AZ31 magnesium alloy

Acknowledgments

References

1. S. Seipp, M.F.X. Wagner, K. Hockauf, I. Schneider, L.W. Meyer, and M. Hockauf, Microstructure, Crystallographic Texture and Mechanical Properties of the Magnesium Alloy AZ31B after Different Routes of Thermo-Mechanical Processing, *Int. J. Plast.*, 2012, **35**, p 155–166.

2. A.A. Luo, Magnesium Casting Technology for Structural Applications, *J. Magnes. Alloy.*, 2013, **1**, p 2–22.

3. G. Zhou, Y. Yang, H. Zhang, F. Hu, X. Zhang, C. Wen, W. Xie, B. Jiang, X. Peng, and F. Pan, Microstructure and Strengthening Mechanism of Hot-Extruded Ultralight Mg-Li-Al-Sn Alloys with High Strength, *J. Mater. Sci. Technol.*, 2022, **103**, p 186–196.

4. Y. Zhou, Q. Luo, B. Jiang, Q. Li, and F. Pan, Strength-Ductility Synergy in Mg98.3Y1.3Ni0.4 Alloy Processed by High Temperature Homogenization and Rolling, *Scr. Mater.*, 2022, **208**, p 114345.

5. K. Fushimi, K. Miyamoto, and H. Konno, Anisotropic Corrosion of Iron in pH 1 Sulphuric Acid, *Electrochim. Acta*, 2010, **55**, p 7322–7327.

6. J. Chen, L. Tan, X. Yu, I.P. Etim, M. Ibrahim, and K. Yang, Mechanical Properties of Magnesium Alloys for Medical Application: A Review, *J. Mech. Behav. Biomed. Mater.*, 2018, **87**, p 68–79.

7. M. Li, A. Seyeux, F. Wiame, P. Marcus, and J. Światowska, Insights on the Al-Cu-Fe-Mn Intermetallic Particles Induced Pitting Corrosion of Al-Cu-Li Alloy, *Corros. Sci.*, 2020, **176**, p 109040.

8. J. Fu and K. Cui, Effect of Mn content on the microstructure and corrosion resistance of Al-Cu-Mg-Mn alloys, *J. Alloys Compd.*, 2022, **896**, p 162903.

9. Y. Zhao, H. Zhang, J. Fan, L. Wang, Q. Zhang, C. Peng, H. Dong, and B. Xu, Grain Refining and Improving Mechanical Properties of AZ31 Mg Alloy Sheets by Multi-Pass Warm Rolling with Falling Temperature, *J. Mater. Res.*, 2018, **33**, p 2827–2834.

10. M. Liu, D. Qiu, M.-C. Zhao, G. Song, and A. Atrens, The Effect of Crystallographic Orientation on the Active Corrosion of Pure Magnesium, *Scr. Mater.*, 2008, **58**, p 421–424.

11. Q. Jiang, X. Ma, K. Zhang, Y. Li, X. Li, Y. Li, M. Ma, and B. Hou, Anisotropy of the Crystallographic Orientation and Corrosion Performance of High-Strength AZ80 Mg Alloy, *J. Magnes. Alloy*, 2015, **3**, p 309–314.

12. C. Li, D. Xu, B. Wang, L. Sheng, and E. Han, Suppressing Effect of Heat Treatment on the Portevin–Le Chatelier Phenomenon of Mg-4% Li-6% Zn-1.2% Y Alloy, *J. Mater. Sci. Technol.*, 2016, **32**, p 1232–1238.

13. H. Su, X. Zhou, S. Zheng, H. Ye, and Z. Yang, Dislocation Facilitated Formation and Evolution of Basal-Prismatic/Prismatic-Basal Interfaces in a Mg Alloy, *Scr. Mater.*, 2022, **206**, p 114237.

14. S.M. Arab and A. Akbarzadeh, The Effect of Equal Channel Angular Pressing process on the microstructure of AZ31 Mg Alloy Strip Shaped Specimens, *J. Magnes. Alloy*, 2013, **1**, p 145–149.

15. G.B. Hamu, D. Eliezer, and L. Wagner, The Relation Between Severe Plastic Deformation Microstructure and Corrosion Behavior of AZ31 Magnesium Alloy, *J. Alloys Compd.*, 2009, **468**, p 222–229.

16. N.N. Aung and W. Zhou, Effect of Grain Size and Twins on Corrosion Behaviour of AZ31B Magnesium Alloy, *Corros. Sci*, 2010, **52**, p 589–594.

17. N. Stanford, A.S. Taylor, P. Cizek, F. Siska, M. Ramajayam, and M.R. Barnett, 10$\bar{1}$2 Twinning in Magnesium-Based Lamellar Microstructures, *Scr. Mater.*, 2012, **67**, p 704–707.

18. D. Sarker and D.L. Chen, Detwinning and Strain Hardening of an Extruded Magnesium Alloy During Compression, *Scr. Mater.*, 2012, **67**, p 165–168.

19. B.J. Wang, D.K. Xu, J.H. Dong, and W. Ke, Effect of the Crystallographic Orientation and Twinning on the Corrosion Resistance of an as-Extruded Mg-3Al-1Zn (wt.%) Bar, *Scr. Mater.*, 2014, **88**, p 5–8.

20. X. Guo, K. Chen, W. Gao, Z. Shen, and L. Zhang, Corrosion Behavior of Alumina-Forming and Oxide Dispersion Strengthened Austenitic 316 Stainless Steel in Supercritical Water, *Corros. Sci.*, 2018, **138**, p 297–306.

21. H. Zhang, G.S. Huang, J.H. Lin, and L.F. Wang, Influence of Annealing Temperature on Microstructure and Properties of Warm-Rolled AZ31 Magnesium Alloy Sheets, *Mater. Sci. Forum*, 2013, **747–748**, p 352–358.

22. W. He, Q. Zeng, H. Yu, Y. Xin, B. Luan, and Q. Liu, Improving the Room Temperature Stretch Formability of a Mg Alloy Thin Sheet by Pre-Twinning, *Mater. Sci. Eng. A*, 2016, **655**, p 1–8.

23. B. Guan, Y. Xin, X. Huang, C. Liu, P. Wu, and Q. Liu, The Mechanism for an Orientation Dependence of Grain Boundary Strengthening in Pure Titanium, *Int. J. Plast.*, 2022, **153**, p 103276.

24. M. Abbas and M. Shafiee, An Overview of Maintenance Management Strategies for Corroded Steel Structures in Extreme Marine Environments, *Mar. Struct.*, 2020, **71**, p 102718.

25. Y. Liu, X. Lei, L. Hao, S. Han, R. Yang, and N. Wang, The Anisotropy Electrochemical Corrosion Behavior of Ni-Based Single Crystal Superalloy on Different Crystal Planes: An Investigation from the Film Growth Aspect, *Appl. Surf. Sci*, 2022, **576**, p 151785.

26. S. Sun, W. Zai, Y. Chen, L. Zhao, G. Sun, J. Hu, S. Han, and J. Lian, Effects of Cold-Rolling and Subsequent Annealing on the Nano-Mechanical and Creep Behaviors of CrCoNi Medium-Entropy Alloy, *Mater. Sci. Eng. A*, 2022, **839**, p 142802.

27. L.-Y. Cui, S.-D. Gao, P.-P. Li, R.-C. Zeng, F. Zhang, S.-Q. Li, and E.-H. Han, Corrosion Resistance of a Self-Healing Micro-Arc Oxidation/Polymethyltrimethoxysilane Composite Coating on Magnesium Alloy AZ31, *Corros. Sci.*, 2017, **118**, p 84–95.

28. H. Fang, S. Zhou, X. Qi, C. Wang, and Y. Tian, A Multifunctional Osteogenic System of Ultrasonically Spray Deposited Bone-Active Coatings on Plasma-Activated Magnesium. J. Magnes. Alloy, (2021)

29. G. Song, A. Atrens, D. Stjohn, J. Nairn, and Y. Li, The electrochemical corrosion of pure magnesium in 1 N NaCl, *Corros. Sci.*, 1997, **39**, p 855–875.

30. Q. Yang, B. Jiang, J. He, B. Song, W. Liu, H. Dong, and F. Pan, Tailoring texture and refining grain of magnesium alloy by differential speed extrusion process, *Mater. Sci. Eng. A*, 2014, **612**, p 187–191.

31. D. Wu, R. Chen, and E. Han, Excellent Room-Temperature Ductility and Formability of Rolled Mg-Gd-Zn Alloy Sheets, *J. Alloys Compd.*, 2011, **509**, p 2856–2863.

32. K. Li, L. Sun, Z. Chen, S. Chen, and W. Li, Failure Analysis of Anion Synergy on Pitting Behavior of Liner 316L in Sour Water System by Electrochemical Tests, *Eng. Fail Anal.*, 2022, **133**, p 105982.

33. K. Moghadasi, M.S.M. Isa, M.A. Ariffin, S. Raja, B. Wu, M. Yamani, M.R. Bin Muhamad, F. Yusof, M.F. Jamaludin, and M.S. Bin Ab Karim, A Review on Biomedical Implant Materials and the Effect of Friction Stir Based Techniques on Their Mechanical and Tribological Properties, *J. Mater. Res. Technol.*, 2022, **17**, p 1054–1121.

34. M. Esmaily, J. Svensson, S. Fajardo, N. Birbilis, G. Frankel, S. Virtanen, R. Arrabal, S. Thomas, and L. Johansson, Fundamentals and Advances in Magnesium Alloy Corrosion, *Prog. Mater. Sci*, 2017, **89**, p 92–193.

35. X. Jia, J. Song, B. Xiao, Q. Liu, H. Zhao, Z. Yang, L. Wu, B. Jiang, A. Atrens, and F. Pan, Influence of Indentation Size on The Corrosion Behaviour of a Phosphate Conversion Coated AZ80 Magnesium Alloy, *J. Mater. Res. Technol.*, 2021, **14**, p 1739–1753.

36. V. Patel, W. Li, J. Andersson, and N. Li, Enhancing Grain Refinement and Corrosion Behavior in AZ31B Magnesium Alloy Via Stationary Shoulder Friction Stir Processing, *J. Mater. Res. Technol.*, 2022, **17**, p 3150–3156.

37. M. Liu, P. Schmutz, P.J. Uggowitzer, G. Song, and A. Atrens, The Influence of Yttrium (Y) on the Corrosion of Mg-Y sBinary Alloys, *Corros. Sci.*, 2010, **52**, p 3687–3701.